Theoretical and experimental examination of the intermediate-band concept for strain-balanced (In,Ga)As/Ga(As,P) quantum dot solar cells

Voicu Popescu, Gabriel Bester,* Mark C. Hanna, Andrew G. Norman, and Alex Zunger
National Renewable Energy Laboratory, Golden, Colorado 80401, USA
(Received 20 August 2008; published 20 November 2008)

The intermediate-band solar cell (IBSC) concept has been recently proposed to enhance the current gain from the solar spectrum whilst maintaining a large open-circuit voltage. Its main idea is to introduce a partially occupied intermediate band (IB) between the valence band (VB) and conduction band (CB) of the semiconductor absorber, thereby increasing the photocurrent by the additional VB→IB and IB→CB absorptions. The confined electron levels of self-assembled quantum dots (QDs) were proposed as potential candidates for the implementation of such an IB. Here we report experimental and theoretical investigations on $In_yGa_{1-y}As$ dots in a $GaAs_{1-x}P_x$ matrix, examining its suitability for acting as IBSCs. The system has the advantage of allowing strain symmetrization within the structure, thus enabling the growth of a large number of defect-free QD layers, despite the significant size mismatch between the dot material and the surrounding matrix. We examine the various conditions related to the optimum functionality of the IBSC, in particular those connected to the optical and electronic properties of the system. We find that the intensity of absorption between QD-confined electron states and host CB is weak because of their localized-to-delocalized character. Regarding the position of the IB within the matrix band gap, we find that, whereas strain symmetrization can indeed permit growth of multiple dot layers, the current repertoire of $GaAs_{1-x}P_x$ barrier materials, as well as $In_yGa_{1-y}As$ dot materials, does not satisfy the ideal energetic locations for the IB. We conclude that other QD systems must be considered for QD-IBSC implementations.

DOI: 10.1103/PhysRevB.78.205321 PACS number(s): 72.40.+w, 73.21.La, 78.67.Hc, 84.60.Jt

I. INTRODUCTION

Conventional solar cells made of a single absorber material can convert to electricity photons with a minimum energy corresponding to the lowest-energy band gap of the absorbing semiconductor, whereas lower-energy photons are practically wasted. A number of ideas have been adopted to overcome this limitation.[1,2] One of them, discussed here, is the intermediate-band solar cell (IBSC).[3] As shown schematically in Fig. 1(a), the idea is to create, in addition to the VB and CB of the absorber material, a partially occupied IB, thus affording sub-band-gap absorption VB→IB into the empty states of the IB (process B), and IB→CB from the occupied states of IB (process C). A few conditions need to be maximized for gaining efficiency from such a concept [Fig. 1(b)]:

(i) The VB→IB and IB→CB excitations must be optically allowed and strong. Thus, the agent creating the IB must have significant concentration and oscillator strength.

(ii) The VB→IB and IB→CB absorption spectra should ideally have no spectral overlap with each other. This "photon-sorting" condition ensures maximum quantum efficiency for given positions of the CB-IB spacing (E_L in Fig. 1) and IB-VB spacing (E_H in Fig. 1).

(iii) Calculations for concentrated light[3] show that the ideal position of the IB should be $E_L \simeq E_c - 0.7$ eV and $E_H \simeq E_v + 1.2$ eV or, conversely, $E_L \simeq E_c - 1.2$ eV and $E_H \simeq E_v + 0.7$ eV.

There are a number of possible deleterious effects [Fig. 1(c)] that need to be minimized:

(a) the capture of matrix CB electrons by the IB (process 1), or the capture of matrix VB holes by the dot (process 4);

(b) the thermal escape of either IB electrons to the CB (process 1′) or of dot holes to the matrix VB (process 4′);

(c) the nonradiative recombination of IB electrons with VB holes (process 2); and

(d) the ever-present recombination of CB electrons with VB holes (process 3) must be as slow as possible.

It has been suggested that the IB be made either by alloying a sublattice into a bulk crystal using an early 3*d* transition metal (TM), e.g., Ti in GaP,[4] Cr in ZnS,[5] and TM in $CuGaS_2$,[6] In_2S_3, and $MgIn_2S_4$,[7] or by employing highly mismatched alloys, such as $Zn_{1-y}Mn_yO_xTe_{1-x}$ (Ref. 8) or $GaN_xAs_{1-y}P_y$.[9]

Here we examine a possible realization of IBSC where the agent creating the IB is an array of (In,Ga)As quantum dots embedded in a Ga(As,P) matrix. Previous realizations of quantum dot (QD)–IBSCs were reported by Luque *et al.*[10] (InAs QDs in GaAs matrix), by Suraprapapich *et al.*[11] (InAs QDs in GaAs/AlGaAs matrix), and by Laghumavarapu *et*

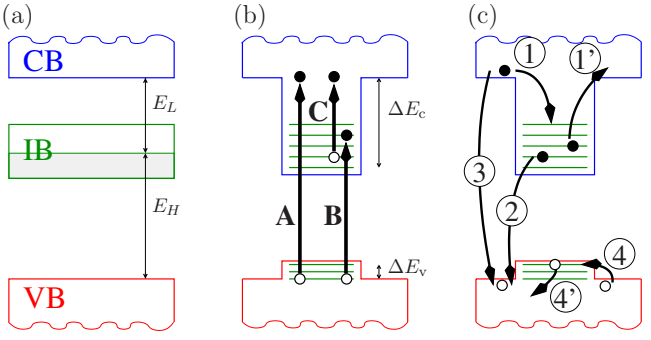

FIG. 1. (Color online) Schematic diagram of single-particle energy levels in a QD array and its equivalent intermediate-band system. (a) Valence band (VB), conduction band (CB), and intermediate band (IB). (b) Desired transitions. (c) Transitions that have deleterious effects.

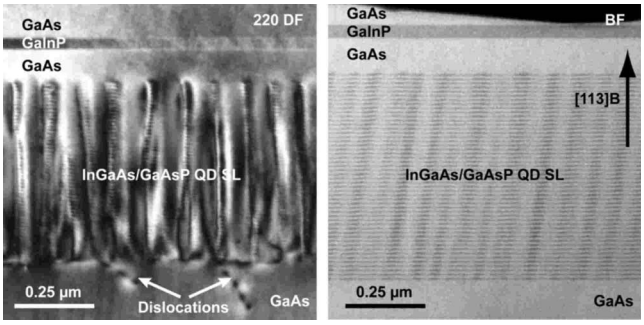

FIG. 2. Left: 220 Dark-field (DF) transmission electron microcopy (TEM) image showing the generation of misfit dislocations in 50-period (In,Ga)As/Ga(As,P) (0.8% P) QD superlattice grown on (113)B GaAs without strain balance. Right: Bright-field (BF) TEM image showing highly uniform 50-period (In,Ga)As/Ga(As,P) (14% P) QD superlattice containing no misfit dislocations grown on (113)B GaAs with strain balance.

al.[12] (GaSb QDs in GaAs), all these using *p*-GaAs as substrate. It is obvious from condition (i) above that to ensure strong VB→IB and IB→CB absorptions, one needs a high concentration of defect-free dots in the matrix. In the Stranski-Krastanov growth, this implies a significant number of layers of dots separated from each other by the barrier material. However, in the applications mentioned above, the number of dot layers was severely limited by the strain accumulated in the system as the number of dot layers is increased. It was recently proposed[13,14] to introduce GaP strain-compensating layers into the GaAs matrix. A higher efficiency of these cells was obtained, but still the number of QD layers was limited. Based on a similar principle, we explore here a strain-symmetrized architecture, allowing the growth of a large number of dot layers.

Having selected a system that ensures strain symmetrization [a step toward condition (i)], we next examine condition (ii) by measuring and calculating the spectra. We find that the intensity of absorption between QD-confined electron states and the host CB is weak because of their localized-to-delocalized character. Regarding condition (iii) we conclude that, whereas strain symmetrization can indeed allow the growth of multiple dot layers, the current repertoire of $GaAs_{1-x}P_x$ barrier materials, as well as $In_yGa_{1-y}As$ dot materials, does not come close to satisfying the ideal energetic locations E_L and E_H for any reasonable x and y. Furthermore, the deleterious condition (a), requiring that the offset ΔE_v between the confined dot hole levels and the matrix valence-band maximum (VBM) be as small as possible, is far from being fulfilled. We conclude that other materials must be considered for QD-IBSC.

II. HOW TO STABILIZE MANY REPEATED LAYERS OF STRAINED DOTS VIA STRAIN SYMMETRIZATION

A key requirement for the QD implementation of IBSCs is the growth of a large number of QD layers. This is needed not only in order to increase the amount of absorbed radiation inside the cell, but also to ensure that a sufficiently large number of QDs lie in the flatband region of the cell where they can act as IB absorbers.[15] The use of self-assembled QDs imposes limitations by the very nature of the Stranski-Krastanov growth process involved.[16] The lattice mismatch between the substrate and the epitaxial layer triggers the QD formation above a critical thickness at which the Stranski-Krastanov transition occurs. While this process leads to regular-sized and similarly shaped QDs, it also has the negative effect of accumulating strain along the growth direction. Attempts of improving the QD-IBSC efficiency[17] using 50 layers of InAs/GaAs QDs failed for this reason: the accumulated strain led to emitter degradation and efficiency drop as compared to a thinner cell of 10 layers of InAs/GaAs QDs.[18] An example of sample deterioration induced by accumulated strain is given in the left panel of Fig. 2. Here we show a TEM image of a 50-period $In_{0.47}Ga_{0.53}As/GaAs_{0.992}P_{0.008}$ QD superlattice grown on a (113)B GaAs substrate. While good-quality QDs are indeed obtained, there is also the appearance of misfit dislocations to be noted.

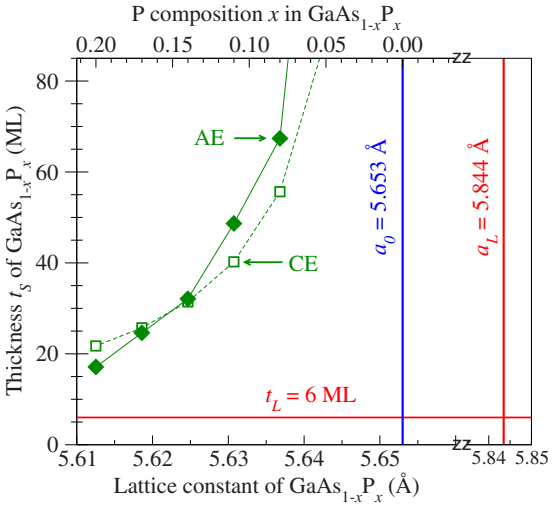

FIG. 3. (Color online) Thickness of $GaAs_{1-x}P_x$ layer necessary to attain the strain-balance condition in an $(In_{0.47}Ga_{0.53}As)_6/(GaAs_{1-x}P_x)_n$ quantum well system on GaAs(001) substrate, as calculated from AE or from CE. Vertical lines mark the natural lattice constants of GaAs, a_0, and of $In_{0.47}Ga_{0.53}As$, a_L. The fixed thickness t_L of the $In_{0.47}Ga_{0.53}As$ quantum well is also shown, with horizontal line.

The problem of strain accumulation in large superlattices may be circumvented by using the well-known concept of strain balance or strain symmetrization.[13,19–22] If a substrate has a lattice constant a_0 and the film grown on it has a lattice constant $a_L > a_0$, then one needs to deposit on the substrate an additional film with natural lattice constant a_S, with $a_S < a_0$. The aim of strain balancing is to chose the thicknesses t_L and t_S of the two film materials so that the sequence of tensile-compressive strain leads to zero overall in-plane stress. In order to predict the desired geometry, one has to calculate the elastic strain energy $E=UV$ of the epitaxial combination of materials L and S, where V is the volume of the sample. The stress and strain tensors $\underline{\sigma}$ and $\underline{\varepsilon}$ are related by

TABLE I. Equilibrium lattice constant a_0; input VFF force constants α, β, and σ [see Eq. (25) of Ref. 25]; and the VFF-calculated elastic constants C_{ij} used in the calculations for GaAs, InAs, GaP, and InP.

	a_0 (Å)	α	β (10^3 dyne/cm)	σ	C_{11}	C_{12} (10^{11} dyne/cm^2)	C_{44}
GaAs	5.6533	32.153	9.370	−4.099	12.11	5.48	6.04
InAs	6.0583	21.674	5.760	−5.753	8.33	4.53	3.80
GaP	5.4505	36.249	10.697	−4.120	14.05	6.20	7.03
InP	5.8687	26.200	6.602	−6.663	10.11	5.61	4.49

$$\underline{\sigma} = \frac{\partial U}{\partial \underline{\varepsilon}} = \frac{1}{V}\frac{\partial E}{\partial \underline{\varepsilon}}. \tag{1}$$

Choosing a frame of reference with its z axis along the growth direction, the in-plane components of the stress tensor $\underline{\sigma}$ can be calculated after imposing the condition that the system is relaxed along z, i.e., that the surface and all the interfaces are stress free.

A. Calculating the strain-balance condition

1. Using continuum elasticity

A relatively simple way to determine the elastic energy E, its density U, and thus the strain-balance condition is provided by continuum-elasticity (CE) theory. Within CE, the condition for strain balance for the (001) growth direction is[19,20]

$$\frac{t_L^{(001)}}{t_S^{(001)}} = -\frac{A_S^{(001)}\varepsilon_\parallel(S)a_L}{A_L^{(001)}\varepsilon_\parallel(L)a_S}, \tag{2}$$

where

$$\varepsilon_\parallel(\alpha) = \frac{a_0 - a_\alpha}{a_0} \quad \text{for} \quad \alpha \equiv L \ \text{or} \ S \tag{3}$$

and

$$A_\alpha^{(001)} = C_{11,\alpha} + C_{12,\alpha} - \frac{2C_{12,\alpha}^2}{C_{11,\alpha}} \quad \text{for} \ (001), \tag{4}$$

with $C_{11,\alpha}$ and $C_{12,\alpha}$ as the elastic constants of the materials L and S. For a given substrate (a_0) the strain-balanced geometry of two epitaxial layers L (a_L) and S (a_S) can be determined, from Eqs. (2)–(4), through the following steps: (1) determine the epitaxial strain $\varepsilon_\parallel(\alpha)$; (2) fix the thickness of one of the layers (e.g., t_L); (3) calculate the coefficients A_α using the available (experimental) elastic constants $C_{ij,\alpha}$; and (4) get the thickness of the second layer (t_S) by solving Eq. (2). If one or both of the materials L and S are alloys, usually a linear dependence on composition is assumed for the lattice constant a_α and elastic constants $C_{ij,\alpha}$.

2. Using atomistic elasticity

One can alternatively calculate directly the elastic energy E and the density U of a system by means of an atomistic-elasticity (AE) model. The method adopted here is the valence force field (VFF) (Refs. 23 and 24) in its generalized version.[25] Within this framework, the system is described by the ensemble of all atoms which are allowed to relax around their (bulk) equilibrium positions. Appropriate boundary conditions can be accounted for by defining a supercell containing the atomic positions. The elastic energy is calculated using the expression

$$E = \sum_i \sum_j^{\text{nn } i} \frac{3}{8}\alpha_{ij}\Delta d_{ij}^2 + \sum_i \sum_{k>j}^{\text{nn } i} \frac{3\beta_{jik}}{8d_{ij}^0 d_{ik}^0}[(\vec{R}_j - \vec{R}_i)\cdot(\vec{R}_k - \vec{R}_i) - \cos\ \theta_{jik}^0 d_{ij}^0 d_{ik}^0]^2 + \sum_i \sum_{k>j}^{\text{nn } i} \frac{3\sigma_{jik}}{d_{ik}^0}\Delta d_{ij}[(\vec{R}_j - \vec{R}_i)\cdot(\vec{R}_k - \vec{R}_i) - \cos\ \theta_{jik}^0 d_{ij}^0 d_{ik}^0]. \tag{5}$$

In this equation, $\Delta d_{ij} = [(\vec{R}_i - \vec{R}_j)^2 - (d_{ij}^0)^2]/d_{ij}^0$, $\vec{R}_i$ is the coordinate of atom i, and d_{ij}^0 is the ideal (unrelaxed) bond distance between atoms i and j. Further, θ_{jik}^0 is the ideal (unrelaxed) angle of the bond j-i-k. The notation $\Sigma^{\text{nn } i}$ denotes summation over the nearest neighbors of atom i. The bond stretching, bond-angle bending, and bond-length/bond-angle interaction terms are described by the VFF parameters α_{ij}, β_{ijk}, and σ_{ijk}, which are related to the elastic coefficients C_{ij} of the corresponding bulk material.[25] For the consistency of the results we have fitted the VFF parameters to the same bulk elastic coefficients C_{ij} of GaAs, GaP, InAs, and InP binary compounds[26,27] used when applying the CE equations. Their values are given in Table I.

The strain-balance condition is then determined following an analogous procedure as above, by keeping one of the materials and its thickness, e.g., L, fixed and varying the composition and the thickness of the second one, S. The elastic energy is calculated using Eq. (5), from which the stress tensor $\underline{\sigma}$ can be obtained by numerical evaluation of the energy gradient entering Eq. (1). The zeros of the in-plane stress provide the thickness t_S corresponding to a strain-balanced t_L/t_S combination. We should note here two important differences with respect to the CE-based procedure: (i) no approximations for the composition dependence of the alloy lattice constants and elastic coefficients are required when performing the VFF-AE calculations; and (ii) as it will be shown below, whereas Eq. (2) gives a unique value for the $t_L^{(001)}/t_S^{(001)}$ ratio, the AE estimations show a slight dependence on the actual thicknesses.

3. Finding strain balance for the $In_{0.47}Ga_{0.53}As/GaAs_{1-x}P_x$ quantum well system

Following the procedure described above, we have determined the strain-balance condition for an

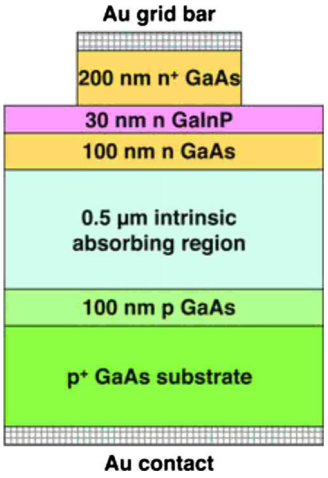

FIG. 4. (Color online) Diagram of the *pin*-type solar cell device structure grown on highly *p*-doped (113)B GaAs substrates used in this work. The 0.5 μm intrinsic absorbing region of the device is formed from a 50-period undoped (In,Ga)As/Ga(As,P) QD superlattice in the QD cell structures and undoped GaAs in the GaAs control sample. The intrinsic region is capped by a 100-nm-thick *n*-doped GaAs layer, a 30-nm-thick high-band-gap *n*-doped (Ga,In)P window layer, and a 200-nm-thick highly *n*-doped GaAs contact layer.

$In_{0.47}Ga_{0.53}As/GaAs_{1-x}P_x$ quantum well (QW) system epitaxially grown on a GaAs substrate of lattice constant a_0 =5.6533 Å. The results obtained here for the strain-balanced QW will be later compared in this section with the actual QD system with similar constituents. The thickness t_L of the $In_{0.47}Ga_{0.53}As$ QW (lattice constant a_L=5.844 Å) was kept fixed at t_L=6 monolayers (ML), which is close to the critical thickness for Stranski-Krastanov growth (5.6 ML) of this alloy on GaAs. The $GaAs_{1-x}P_x$ (playing the role of material *S*) barrier was taken with varying P content *x*. At each *x*, for different thicknesses t_S, Eq. (1) was evaluated for a number of ten different random-alloy realizations. The corresponding results of AE in-plane zero stress are shown in Fig. 3 with solid symbols. For comparison, results obtained using the CE formula [Eq. (2)] are also shown, with open symbols.

Figure 3 shows how strain balance works: because the lattice constant a_L and thickness t_L of $In_{0.47}Ga_{0.53}As$ (material *L*) are fixed, the corresponding lattice mismatch with the substrate (a_0) and the compressive strain and stress are also fixed. As the P composition *x* in the $GaAs_{1-x}P_x$ barrier increases, its lattice constant $a_S(x)$ decreases. This results in an increased lattice mismatch and thus an increased tensile strain in the barrier. Consequently, the thickness t_S necessary to have an in-plane tensile stress which exactly compensates for the compressive stress in the QW decreases with increasing lattice mismatch and P composition. This characteristic is common to both AE and CE $t_S(x)$ functions shown in Fig. 3. In an interval between x=0.12 and x=0.18, the two values $t_S^{AE}(x)$ and $t_S^{CE}(x)$ are very close, being actually equal around x=0.15.

We applied the same procedure to different QW systems made of pure binaries: $(GaP)_{n_1}/(InAs)_{n_2}$ on GaAs(001) and $(InAs)_{n_1}/(GaAs)_{n_2}$ on InP(001), with n_1 kept fixed and different values of n_2. The results of these strain-balance calculations are presented in Table II. The AE results show the slight dependence on the actual fixed thickness n_1a_1 mentioned above. It can be seen that overall agreement as good as 1% between CE and AE results was achieved for the (001) substrate orientation. In contrast, comparing the CE and AE results for the $In_{0.47}Ga_{0.53}As/GaAs_{1-x}P_x$ QW, we note big differences (10% and more) outside the small composition interval mentioned above. This might be caused by the linear approximation used for the dependence of elastic coefficients on *x* when applying the CE formula.

TABLE II. Comparison of the strain-balance conditions as obtained using the AE- and CE-based procedures for the nonalloy quantum well systems $(GaP)_{n_1}/(InAs)_{n_2}$ and $(InAs)_{n_1}/(GaAs)_{n_2}$ on different substrates. In all the calculations n_1 was fixed and n_2 was varied in order to attend the strain balance. In applying the AE-based procedure, several values of n_1 were considered. The CE-based formulas, Eqs. (2) and (6), show no dependence on the actual thicknesses involved.

n_1		n_2a_2/n_1a_1	
QW system:		$(GaP)_{n_1}/(InAs)_{n_2}$	$(InAs)_{n_1}/(GaAs)_{n_2}$
Substrate:		GaAs	InP
	5	1.1274	0.4853
	20	1.1550	0.4870
	30	1.1583	0.4875
(001)	CE	1.1488	0.4809
	5	0.9607	0.5866
	20	0.9905	0.5841
	30	0.9939	0.5840
(111)	CE	1.0173	0.5351

4. Strain balance for general orientation of the substrate

Deriving the strain-balance condition in the case of higher-index substrates can be done by introducing a new (primed) frame of reference,[28] with its z' axis parallel to the growth direction. The unitary transformation between the two frames of reference can be applied either to the strain tensor or to the elastic constants, providing a generalized expression for the elastic energy in the primed reference system. This expression then enables one, analogously to the (001) orientation, to derive a strain-balance condition in the new frame of reference. We illustrate below this generalization for two orientations.

In the case of a (111)-oriented substrate (single shear component), we obtain an expression analogous to Eq. (2):

$$\frac{t_L^{(111)}}{t_S^{(111)}} = -\frac{A_S^{(111)}\varepsilon_{\parallel}(S)a_L}{A_L^{(111)}\varepsilon_{\parallel}(L)a_S}, \tag{6}$$

with

$$A_\alpha^{(111)} = \frac{C_{11,\alpha}+C_{12,\alpha}+C_{14,\alpha}}{2} - \frac{2}{3}\frac{(C_{11,\alpha}+2C_{12,\alpha}-2C_{44,\alpha})^2}{C_{11,\alpha}+2C_{12,\alpha}+4C_{44,\alpha}} + \frac{C_{11,\alpha}+5C_{12,\alpha}-2C_{44,\alpha}}{6} \quad \text{for (111)}, \tag{7}$$

and $\varepsilon_{\parallel}(\alpha)$ referring to the (111) in-plane epitaxial strain.

We compare in Table II the AE strain-balance predictions for the two pure binaries QW epitaxial systems $(GaP)_{n_1}/(InAs)_{n_2}$ on GaAs(111) and $(InAs)_{n_1}/(GaAs)_{n_2}$ on InP(111) compared with the CE estimation, Eq. (6). We used the same VFF force constants and elastic coefficients as for the (001) direction, listed in Table I. As in the case of the (001)-oriented substrate, the AE results depend on the thickness n_1a_1 of the layer kept fixed. One can also see that the estimations of strain-balanced n_2a_2/n_1a_1 ratio obtained using the CE-derived condition are about 2–9 % off the direct AE calculations.

For some orientations, such as (110), the stress tensor is not isotropic, i.e., $\sigma_{x'x'} \neq \sigma_{y'y'}$ even in the case of an isotropic strain.[28] Moreover, for substrates with indices other than (100), (111), and (110), the shear-stress components are nonzero.[29,30] Consequently, they have to be likewise zeroed to achieve a strain-balanced configuration. Setting the strain-balance condition in the general case leads merely to a homogeneous system of equations rather than a single equation. Depending on the elastic coefficients and thus on the materials involved, this homogeneous system might or might not admit a nontrivial solution.

For the (110)-oriented substrate, imposing the simultaneous conditions of zero $\sigma_{x'x'}$ and $\sigma_{y'y'}$, one needs to solve for $t_L^{(110)}$ and $t_S^{(110)}$ the homogeneous system of equations

$$\begin{cases} P_L\varepsilon_{\parallel}(L)t_L^{(110)} + \dfrac{a_L}{a_S}P_S\varepsilon_{\parallel}(S)t_S^{(110)} = 0 \\ Q_L\varepsilon_{\parallel}(L)t_L^{(110)} + \dfrac{a_L}{a_S}Q_S\varepsilon_{\parallel}(S)t_S^{(110)} = 0, \end{cases} \tag{8}$$

which admits the nontrivial solution only if

$$\frac{P_L}{Q_L} = \frac{P_S}{Q_S}, \tag{9}$$

in which case one obtains

$$\frac{t_L^{(110)}}{t_S^{(110)}} = -\frac{P_S\varepsilon_{\parallel}(S)a_L}{P_L\varepsilon_{\parallel}(L)a_S}. \tag{10}$$

In Eqs. (8)–(10), the quantities P_α and Q_α are given respectively by

$$P_\alpha = \frac{4C_{44,\alpha}(C_{11,\alpha}+2C_{12,\alpha})}{C_{11,\alpha}+C_{12,\alpha}+2C_{44,\alpha}},$$

$$Q_\alpha = \frac{C_{11,\alpha}^2 - 2C_{12,\alpha}^2 + C_{11,\alpha}C_{12,\alpha} + 2C_{11,\alpha}C_{44,\alpha} + 4C_{12,\alpha}C_{44,\alpha}}{C_{11,\alpha}+C_{12,\alpha}+2C_{44,\alpha}}$$

$$\text{for (110)}. \tag{11}$$

Using the elastic constants given in Table I, no analytical strain-balance solution can be found for the two pure binaries QW epitaxial systems $(GaP)_{n_1}/(InAs)_{n_2}$ on GaAs(110) and $(InAs)_{n_1}/(GaAs)_{n_2}$ on InP(110). In agreement with the CE predictions, the AE calculations also failed in finding a solution for a wide range of n_1. This result by no means rules out the possibility of actually finding a (110)-oriented strain-balanced combination. It simply shows that the quantity

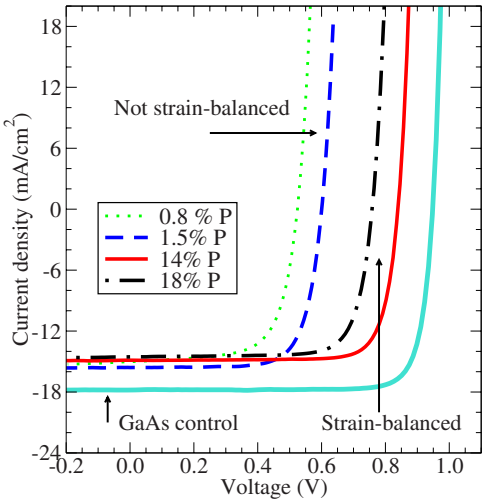

FIG. 5. (Color online) Light current-voltage measurements at room temperature for 50-period undoped $In_{0.47}Ga_{0.53}As/GaAs_{1-x}P_x$ QD superlattice cells containing different concentrations of P in the barrier layers: 0.8% (green dotted line), 1.5% (blue dashed line), 14% (red solid line), and 18% (black dot-dashed line). All QD cells exhibit lower open-circuit voltage, short-circuit current density, and efficiency than those of the GaAs control cell [cyan (gray) solid line]. Among the QD cells, however, the strain-balanced sample with $x=0.14$ (red solid line) is characterized by the highest open-circuit voltage and efficiency.

$$R_\alpha \equiv \frac{P_\alpha}{Q_\alpha} = \frac{4C_{44,\alpha}(C_{11,\alpha}+2C_{12,\alpha})}{C_{11,\alpha}^2 - 2C_{12,\alpha}^2 + C_{11,\alpha}C_{12,\alpha} + 2C_{11,\alpha}C_{44,\alpha} + 4C_{12,\alpha}C_{44,\alpha}}$$

$$\text{for (110)} \tag{12}$$

should be the same for the materials used for the two layers, $\alpha=L,S$. For the binary systems considered here, the values of the elastic constants given in Table I lead to $R(GaP)=0.0062$, $R(InP)=0.0743$, $R(GaAs)=0.0207$, and $R(InAs)=0.1947$. It is then obvious that achieving strain balance on a (110) substrate requires a careful engineering of the elastic constants, e.g., by alloying. Seeking a numerical solution of the problem might prove to be more advantageous in this case.

B. Growth of $In_{0.47}Ga_{0.53}As$ quantum dots in $GaAs_{1-x}P_x$ matrix on GaAs substrate

We grew by low-pressure metal-organic vapor-phase epitaxy (MOVPE) *pin*-type QD solar cell structures with intrinsic absorbing regions containing 50 layers of nominally 6.1-ML-thick $In_{0.47}Ga_{0.53}As$ QDs separated by ≃10-nm-thick $GaAs_{1-x}P_x$ barrier layers on *p*-type (113)B GaAs substrates. A schematic of the device structure is shown in Fig. 4. Triethylgallium, trimethylindium, arsine, and phosphine were used as sources and the growth temperature was 550 °C. Annealing under H_2 for 30 s after the growth of each InGaAs QD layer was found to be essential in order to grow QD superlattices containing QDs with good size uniformity and

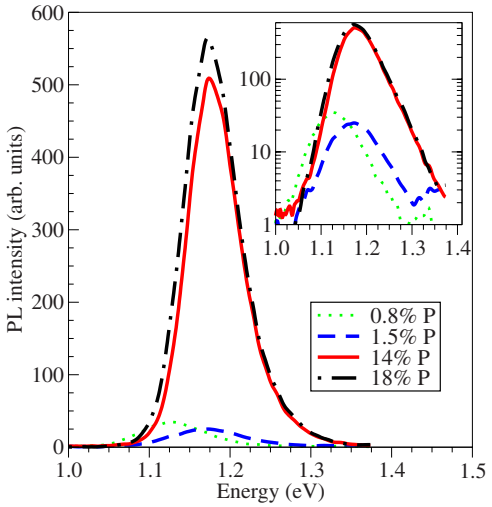

FIG. 6. (Color online) Room-temperature PL spectra obtained from 50-period undoped $In_{0.47}Ga_{0.53}As/GaAs_{1-x}P_x$ QD superlattice cells containing different concentrations of P in the barrier layers: 0.8% (green dotted line), 1.5% (blue dashed line), 14% (red solid line), and 18% (black dot-dashed line). Note that the two samples close to strain balance ($x=0.14$ and $x=0.18$) exhibit an order-of-magnitude greater PL intensity than the two unbalanced ($x=0.008$ and $x=0.015$) QD samples. The inset shows the PL spectra on a logarithmic scale and a reduced energy interval.

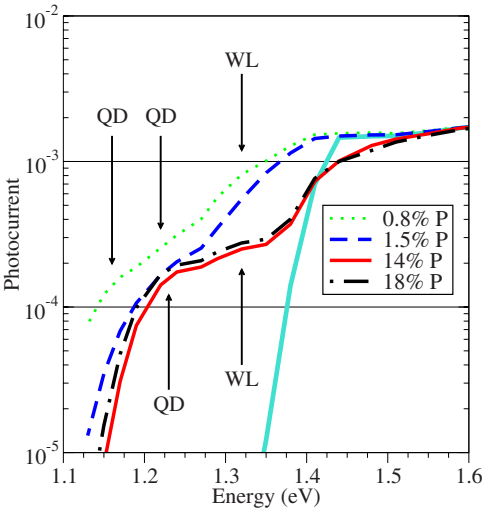

FIG. 7. (Color online) Room-temperature PC spectra obtained from 50-period undoped $In_{0.47}Ga_{0.53}As/GaAs_{1-x}P_x$ QD superlattice cells containing different concentrations of P in the barrier layers: 0.8% (green dotted line), 1.5% (blue dashed line), 14% (red solid line), and 18% (black dot-dashed line). The PC spectra of the QD samples are normalized to the maximum PC of a GaAs control sample [cyan (gray) solid line]. Peaks are observed corresponding to absorption by two QD levels and also to the wetting layer (WL) (see arrows in figure).

regular columns of QDs aligned a few degrees off the [113]B growth direction.[31]

The P content in the $GaAs_{1-x}P_x$ barrier layers was varied from ~0.8% to ~18% by increasing the phosphine flow during growth. The phosphine flow required for achieving the required $GaAs_{1-x}P_x$ barrier layer compositions was determined by first growing a series of calibration layers on (001) GaAs substrates whose P concentrations were then deduced from x-ray-diffraction measurements.

Our AE strain-balance calculations predict for the $GaAs_{1-x}P_x$ barrier with $x=0.14$ a thickness t_S of 32–33 ML. The right panel of Fig. 2 shows a bright-field TEM image of a 50-period QD superlattice. The QDs consist of the same alloy, $In_{0.47}Ga_{0.53}As$, as the ones in the left panel of Fig. 2. Also the substrate is the same. The former, however, are grown in a $GaAs_{0.86}P_{0.14}$ barrier meant to strain balance the superlattice and thus enable a good-quality, defect-free growth. As obvious from the right panel of Fig. 2, this is indeed achieved. Further measurements, to be shown in Sec. III, confirmed that this 50-period QD superlattice with $In_{0.47}Ga_{0.53}As$ as dot material and $GaAs_{0.86}P_{0.14}$ as barrier is indeed at (or very close) to strain balance. The estimated thickness of the $GaAs_{0.86}P_{0.14}$ for the sample shown in the right panel of Fig. 2 was 10.4 nm, which corresponds to about 37 ML of $GaAs_{0.86}P_{0.14}$, a result which is in very good agreement with the theoretical strain-balance prediction in Fig. 3.

III. EXPERIMENTAL CHARACTERIZATION OF THE SAMPLES

A. Current-voltage measurements

The QD cell device wafers were processed into an array of small isolated mesa-type devices with a 2-mm-diameter circular active region. Light current-voltage (*I-V*) measurements were made on several cells from each processed wafer. These measurements were performed at 25 °C under an AM1.5G spectrum at an irradiance of 1000 W/m^2 using an XT10 solar simulator. A Si reference cell was used to calibrate the illumination level.

Typical cell results obtained from four 50-period $In_{0.47}Ga_{0.53}As/GaAs_{1-x}P_x$ device wafers containing 0.8%, 1.5%, 14%, and 18% P in the barrier layer are shown in Fig. 5 together with the results from a control sample of the same device structure (Fig. 4) except that no QDs were included in the undoped GaAs intrinsic region. *Strain-balance improves* the open-circuit voltage V_{oc}: the QD cells containing 0.8% and 1.5% P, which are not strain balanced, exhibited much lower V_{oc}, between ≃0.53 and 0.6 V, than the cells containing 14% and 18% P, between ≃0.76 and 0.84 V, which are close to strain balance. The large increase in V_{oc} of the strain-balanced QD cells in comparison to the non-strain-balanced cells arises for several reasons. The first is that the strain-balanced QD cells contain much lower densities of dislocations [Fig. 2 (right panel)], and hence experience much reduced recombination resulting in higher V_{oc}. The second reason is that increasing the P concentration in the barrier layers to achieve strain balance also increases the average band gap of the intrinsic region that leads to an increase in V_{oc}.

Disappointingly, all the QD superlattice cells exhibited lower V_{oc} than that of the undoped GaAs control cell, 0.95 V. One of the causes of this is due to the VB offset between the $In_{0.47}Ga_{0.53}As$ QDs and the $GaAs_{1-x}P_x$ barrier layers and will be discussed in Sec. IV C.

The V_{oc} of the $In_{0.47}Ga_{0.53}As/GaAs_{1-x}P_x$ QD superlattice cell containing 18% P, 0.76 V, is lower than that of the QD

TABLE III. Experimental peak positions (in eV) obtained from the room-temperature PL and photocurrent (PC) measurements. PL FWHM is also given, expressed in meV. The PL and first PC peaks are assigned to the fundamental excitonic transition. The second peak in PC is ascribed to the intradot $e_{1,2}$-$h_{1,2}$ (P-P) transition.

	PL		PC	
x(P)	Peak (eV)	FWHM (meV)	QD 1 (eV)	QD 2 (eV)
0.008	1.13	100	1.16	1.22
0.015	1.17	100	1.22	
0.140	1.18	75	1.23	
0.180	1.17	79	1.22	

cell containing 14% P, 0.84 V, resulting in a reduced cell efficiency. This may reflect that the cell containing 18% P is no longer strain balanced and contains a higher density of dislocations, resulting in increased recombination and a reduced V_{oc} and efficiency. It can thus be concluded that the cell containing 14% P in the barrier layers is probably the closest to strain balance in the investigated samples.

As in the case of the open-circuit voltage, the short-circuit current density J_{sc} and the efficiencies of the QD cells are also lower than those of the undoped GaAs control cell. The J_{sc} of all the QD cells was fairly similar, 14.5–15.6 mA/cm^2, compared to the J_{sc} of about 17.8 mA/cm^2 measured for the GaAs control cell. The reduced J_{sc} of the QD cells probably results from increased recombination in the QD structures. One would expect the recombination to be increased in the QD samples containing 0.8% and 1.5% P due to the increased density of dislocations in these non-strain-balanced QD superlattices. However, for the samples containing 14% and 18% P, any increase in J_{sc} resulting from a reduction in recombination due to the presence of dislocations may be offset by a reduction in J_{sc} associated with an increase in the average band gap of the intrinsic region and an increase in recombination in the QDs resulting from a stronger electron confinement.

B. Photoluminescence and photoconductivity measurements

Photoluminescence (PL) measurements were performed on all the QD cell structures at room temperature (RT) using the 632.8 nm line of a He/Ne laser and an InGaAs photodiode array as a detector. The spectra are shown in Fig. 6 and the QD peak energies and full width at half maximum (FWHM) are listed in Table III. Low-temperature (77 K) PL data on these samples were reported previously.[32] The main trends in the PL results are that the QD PL peak energy is higher and the PL peak width is narrower for the samples containing increased amounts of P in the barrier layers. The QD PL peak intensity of the higher-P-content, close-to-strain-balanced (In,Ga)As/Ga(As,P) QD samples is an order of magnitude greater than that measured for the non-strain-balanced samples. The reason for the increased PL peak energy will be discussed later in Sec. V. The increased PL peak intensity and narrower peak width observed for the higher-P-content, close-to-strain-balanced InGaAs/GaAsP QD samples are most likely a result of the much lower dislocation density and narrower QD size distribution in the strain-balanced QD samples as compared to the non-strain-balanced samples.

PC spectroscopy measurements[33,34] of the $In_{0.47}Ga_{0.53}As/GaAs_{1-x}P_x$ QD *pin* solar cells and the GaAs control cell were performed at room temperature under normal-incidence unpolarized light at 0 V applied bias. Electron-hole pairs generated in the QDs by interband absorption escape from the QDs, by mainly thermal excitation at room temperature, and form the measured photocurrent. At temperatures greater than $\simeq$200 K, most of the carriers created by interband absorption are expected to escape from the QDs before they recombine and contribute to the photocurrent.[33,34] As a result, it is expected that the PC spectra will give a good representation of the absorption spectra of the QD samples. The measurement system used, constructed for accurately measuring the external quantum efficiency of solar cells, consisted of a tungsten light source, monochromator, optical chopper, and a lock-in amplifier for detection of device currents.

The results are illustrated in Fig. 7, which shows a plot of normalized (to the maximum value of photocurrent for the GaAs control cell) logarithmic photocurrent versus photon energy in eV for each device. It can be seen that all the QD devices display photocurrent at energies less than the GaAs control cell arising from absorption by the QDs and wetting layers. A number of features are visible on the curves (see arrows in Fig. 7) that correspond to absorption transitions associated with the QDs and two-dimensional wetting layers present in the samples. The energies of the transitions that can be clearly distinguished are given in Table III. These transition-energy values were deduced from the experimental curves after first subtracting a linear interpolation of the background signal from the PC spectra in the region of the transitions as described in Ref. 34. It can be seen that the trend in the energy of the first QD transition is similar to that observed for the room-temperature PL results in that it first increases with increasing P content in the barrier layers of the samples but then reaches a constant value of $\simeq$1.22 eV. For the sample with 0.8% P, a higher-energy QD transition is also visible at an energy of $\simeq$1.22 eV. For three of the samples an absorption transition corresponding to the two-dimensional InGaAs wetting layers can also be clearly discerned at 1.32 eV. Comparing the PC results with the PL results in Table III, it is clear that the QD transition energies measured by PC are consistently between 30 and 50 meV higher than those measured by PL. This difference in energy between room-temperature PC and PL results, termed the Stokes shift, has been noted previously and attributed to a thermal carrier redistribution between QDs at room temperature that leads to the energy of the QD PL being redshifted to lower energies.[33,35] For the samples containing 0.8% and 1.5% P, the PC signal starts to drop at a lower energy, $\simeq$1.40 eV, than the GaAs control device, which suggests that a small amount of In may be incorporated in the $GaAs_{1-x}P_x$ barrier layers during growth, leading to a band gap less than that of GaAs. Conversely, for the samples containing 14% and 18% P, the PC signal starts to drop at a

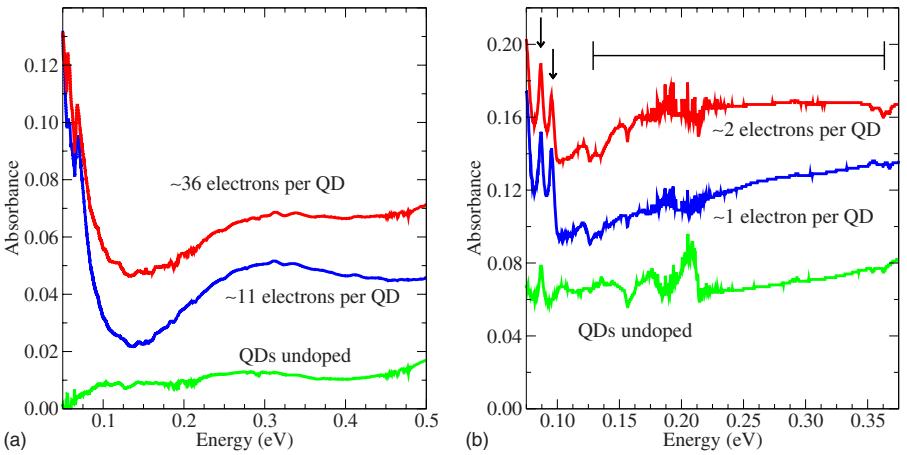

FIG. 8. (Color online) FTIR absorption spectra, obtained from undoped and *n*-doped 50-period $In_{0.47}Ga_{0.53}As(6.1\ ML)/GaAs_{0.86}P_{0.14}(10\ nm)$ strain-balanced QD superlattices grown on undoped (113)B GaAs substrates. (a) FTIR spectra of heavily doped QDs and undoped QDs obtained using normal-incidence light, single pass through QDs. The strong absorbance for the doped QDs at low energies, peaking below the low-energy cutoff of the detector, is believed to be due to intraband absorption. A broader absorbance peak at ~0.3 eV is also present for the doped QDs. (b) FTIR spectra of lightly doped and undoped QDs obtained using light in multipass waveguide configuration. The arrows mark sharp absorption peaks arising from the substrate. The horizontal bar indicates a weak broad absorption peak that is present only for the doped QDs.

higher energy, ≃1.51 eV, reflecting the increase in band gap of the $GaAs_{1-x}P_x$ barrier layers at higher P contents.

C. Fourier-transform infrared-absorption measurements

In order to investigate absorption from the occupied states of the QD intermediate band to the conduction band, process C in Fig. 1(b), a series of undoped and *n*-doped 50-period strain-balanced $In_{0.47}Ga_{0.53}As(6.1\ ML)/GaAs_{0.86}P_{0.14}(10\ nm)$ QD superlattices was grown on semi-insulating (113)B GaAs substrates for Fourier-transform infrared (FTIR) spectroscopy measurements. Samples ($\sim 1\times \sim 0.5\ cm^2$) for FTIR were prepared in a multipass waveguide geometry with polished back surfaces and 45° polished end facets to aid light input and output and enable approximately 20 light passes through the QD layers to enhance the absorption.[36] The FTIR measurements were made at room temperature using unpolarized light in a Nicolet Magna 550 spectrometer using a broadband infrared glow bar source and a deuterated triglycine sulfate (DTGS) detector. Two series of samples were grown: in the first series, two QD superlattices were grown containing doping levels of $6\times 10^{17}\ cm^{-3}$ Si and $2\times 10^{18}\ cm^{-3}$ Se in the $In_{0.47}Ga_{0.53}As$ QDs. For the typically observed QD density of $\sim 10^{10}\ cm^{-2}$, this corresponds to approximately 11 and 36 electrons per QD, respectively. In the second series, two QD superlattices were grown containing doping levels of 3.6×10^{17} and $7.2\times 10^{17}\ cm^{-3}$ Si in 1 ML of the $In_{0.47}Ga_{0.53}As$ QDs. For the same observed QD density of $\sim 10^{10}\ cm^{-2}$, this corresponds to approximately one and two electrons per QD, respectively.

Figure 8(a) illustrates FTIR results obtained from an undoped QD sample and the first series of heavily doped QDs with normal-incidence light passing once through the QD layers. The spectra have been vertically offset for clarity. The absorbance was calculated from

$$A = \log \frac{T_{\mathrm{GaAs}}}{T_{\mathrm{Sample}}}, \tag{13}$$

where T_{GaAs} and T_{Sample} are the light intensities transmitted through an undoped (113)B GaAs substrate reference waveguide and the QD sample waveguide, respectively. A strong absorbance, which peaks at an energy value below the 0.05 eV cutoff of the detector used, is observed for the doped QD samples and is believed to correspond to intraband absorption (see below). The absorption goes through a minimum for the doped QD samples at ~0.13 eV and then rises again at higher energies to a broad and weak peak at ~0.3 eV, thought to be due to absorption transitions between QD-confined levels and the GaAsP barrier layer conduction-band continuum. Shown in Fig. 8(b) are the FTIR results obtained from light incident in the multipass waveguide configuration from the undoped and more lightly doped QD superlattice samples. The spectra have again been offset vertically for clarity. The absorption from the doped samples shows a sharp rise at low energies, peaking at an energy less than the 0.075 eV cutoff of the experiment, believed to correspond to intersubband absorption. Sharp peaks at ~0.087 and ~0.095 eV [arrowed in Fig. 8(b)] are also present for the doped QD samples but are thought to originate from the GaAs substrate.[37] A broad weak absorption feature between ~0.125 and ~0.375 eV (indicated by horizontal bar) also appears for the doped QD samples and is considered to arise from transitions between QD-confined levels and the GaAsP barrier layer conduction-band continuum.

IV. CALCULATING THE ELECTRONIC STRUCTURE OF (In,Ga)As/Ga(As,P) QD ARRAYS

Sections II and III dealt with the problem of designing a strain-balanced $In_{0.47}Ga_{0.53}As/GaAs_{1-x}P_x$ QD-IBSC system. We found that at a P composition of $x=0.14$, a QD superlat-

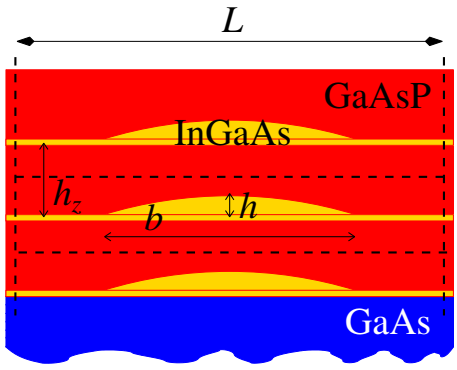

FIG. 9. (Color online) Schematic drawing of the geometry used in the calculations of the $In_yGa_{1-y}As/GaAs_{1-x}P_x$ system. The supercell (dashed-line rectangle) has dimensions $h_z=12.4$ nm and $L=120a_0$, where $a_0=5.653$ Å is the GaAs lattice constant. The dots [yellow (light) area] have a lens shape with diameter $b=40$ nm and height $h=4$ nm. The thickness of the wetting layer is 2 ML.

tice of very high quality can be grown. The beneficial role of balancing the strain in the structure was also seen in the *I-V* characteristic and photoluminescence response of the samples, comparing the results at and off the strain-balance matrix composition.

We will investigate in the following the electronic structure of this system. Our approach uses an atomistic pseudopotential (PP) method that accounts for the proper symmetry of the dot, strain and alloying effects, multiband and multivalley coupling, and spin-orbit interaction.[38] The method will be briefly reviewed below. We will then consider as a benchmark the QD system $In_{0.47}Ga_{0.53}As/GaAs_{0.86}P_{0.14}$ and discuss in detail its electronic structure. After analyzing the different level offsets in view of the IB conditions, we will extend the discussion to the more general $In_yGa_{1-y}As/GaAs_{1-x}P_x$ QD system. Keeping the geometry unchanged, we will vary the matrix (x) and dot (y) compositions. The effects of these modifications on the electronic structure and absorption spectra will be shown and compared with the experimental findings.

A. Method of calculating the electronic structure

We construct a supercell containing all the ingredients of the dot-matrix-substrate we want to describe, as shown in Fig. 9. The QD is considered to be lens shaped, with a diameter $b=40$ nm and a height $h=4$ nm. These values, as well as the barrier thickness (vertical dot separation) $h_z=12.4$ nm, were chosen to match the geometrical parameters of the grown samples. A WL of 2 ML thickness was also included in the structure. The in-plane size of the supercell is $L=120a_0$, with a_0 as the GaAs natural lattice constant. This results in a lateral dot-dot separation of $\simeq 28$ nm, somehow smaller than the experimental one, but sufficiently large to ensure a lateral decoupling of the dots, as it will be shown below. The presence of the GaAs substrate is accounted for by epitaxially matching the $In_yGa_{1-y}As$ and $GaAs_{1-x}P_x$ to a_0. We relax all atomic positions within a fixed simulation cell to achieve minimal strain inside the supercell, where the strain energy is given by the VFF functional [Eq. (5)] discussed in Sec. II.[25]

Once a relaxed configuration is obtained, we place on each atom α=In, Ga, As, and P a screened atomic pseudopotential that depends on the identity α of the atom and the local strain $\underline{\varepsilon}$:

$$v_\alpha(\vec{r},\underline{\varepsilon}) = v_\alpha(\vec{r},0)[1 + \gamma_\alpha \,\mathrm{Tr}(\underline{\varepsilon})], \tag{14}$$

with γ_α a fitting parameter introducing a further dependence on the identity of the neighbors.[38] The unstrained pseudopotential $v_\alpha(\vec{r},0)$ is determined by requiring that the bulk binaries described by $v_\alpha(\vec{r},0)$ fit experimental and local-density-approximation (LDA) data. Furthermore, for each pair AB/AC of binaries, the alloy bowing parameter of the ABC alloy band gap is also fitted. All the pseudopotential parameters used in this work are given in the Appendix.

With the pseudopotential of each atom α and the relaxed positions $\vec{R}_{n\alpha}$, we solve the single-particle equation

$$\left[-\frac{\beta}{2}\nabla^2 + \sum_{n,\alpha} \hat{v}_\alpha(\vec{r} - \vec{R}_{n\alpha}, \underline{\varepsilon}_n) + \hat{V}_{\mathrm{NL}}\right]\psi_i(\vec{r}) = E_i\psi_i(\vec{r}), \tag{15}$$

where $\hat{V}_{\mathrm{NL}}$ represents the nonlocal spin-orbit coupling potential and β is a scaling factor for the kinetic energy[38] (taken to be 1.23 throughout this work). We use a basis set for $\psi_i(\vec{r})$ consisting of a strain-dependent linear combination of bulk bands[39] (LCBB) $u^{\lambda}_{\nu,\vec{k}}(\vec{r},\underline{\varepsilon})$ of band index ν and wave vector $\vec{k}$ of materials $\lambda \equiv$ GaAs, InAs, GaP, and InP. We use $\nu=2,3,4$ (the three bulk Γ_{15v} bands) and a $6\times6\times8$ k mesh for the hole states and $\nu=5$ (the bulk Γ_{1c} band) on a $8\times8\times10$ k mesh for the electron states, which ensured a 1 meV convergence of the hole and electron eigenstates E_i^h and E_i^e. Strain modifications were accounted for in the InAs and GaP basis sets. For the former we took the average strain inside the dot, whereas for the latter we considered the average strain inside the matrix, calculated at a central position between the dots.

Within a single-particle picture, the dipole matrix elements between an initial state $|\psi_i\rangle$ and a final state $|\psi_j\rangle$,

$$M_{ij} = \langle\psi_j|\hat{\vec{r}}|\psi_i\rangle, \tag{16}$$

will be used to calculate the IB→CB and VB→IB absorption spectra (see below). Assuming the IB formed by the first dot-confined electron level (e_0), the IB→CB (VB→IB) involves e_0 as initial (final) state. The corresponding absorption coefficients are then, respectively,

$$\sigma^{\mathrm{IB}\to\mathrm{CB}}(E) \propto \sum_{j>0} |M_{0j}^{ee}|^2 \delta(E_j^e - E_0^e - E), \tag{17}$$

$$\sigma^{\mathrm{VB}\to\mathrm{IB}}(E) \propto \sum_{j\geq0} |M_{j0}^{he}|^2 \delta(E_0^e - E_j^h - E), \tag{18}$$

with $E=\hbar\omega$ as the energy of the absorbed photon. The final (initial) states for $\sigma^{\mathrm{IB}\to\mathrm{CB}}$ ($\sigma^{\mathrm{VB}\to\mathrm{IB}}$) are all the electron (hole) states with energy higher (lower) than e_0.

Knowledge of single-particle eigenstates and eigenvalues enables us to calculate the excitonic energies, for which we

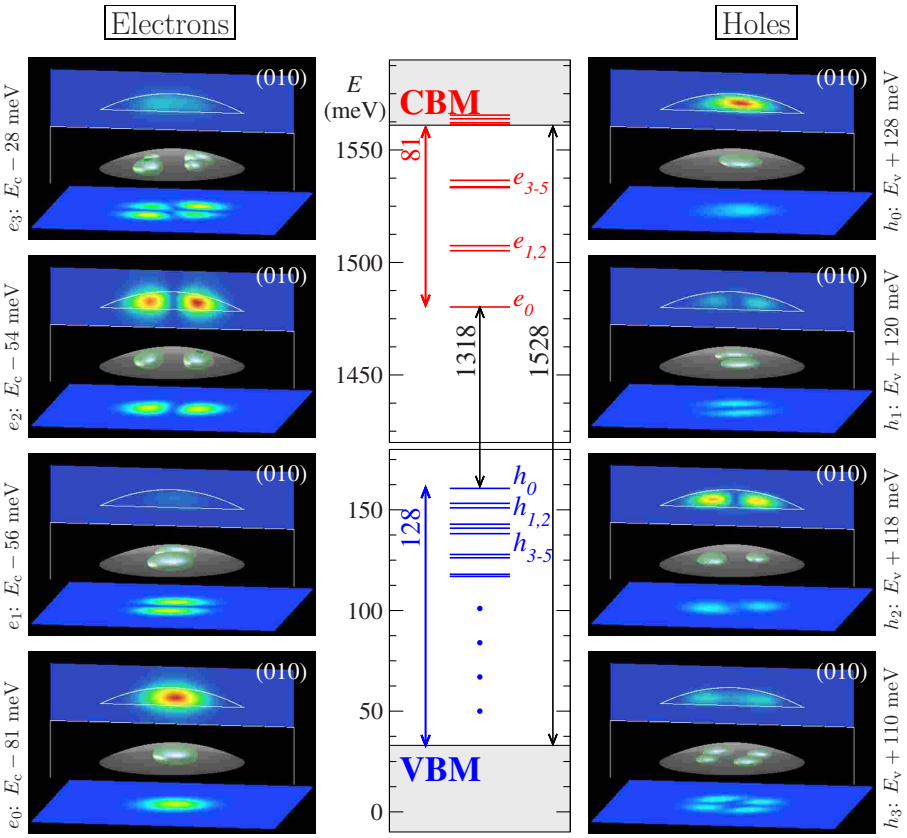

FIG. 10. (Color online) Calculated single-particle energy levels for the QD-IBSC consisting of an $In_{0.47}Ga_{0.53}As$ lens-shaped dot of diameter $b=40$ nm, height $h=4$ nm, and vertical separation $h_z=12.4$ nm. The matrix of the system is $GaAs_{0.86}P_{0.14}$ on GaAs substrate. The energy zero corresponds to GaAs VBM. Only the first ten (Kramers degenerate) levels are shown for electrons and holes. Lower-lying dot-confined hole levels above the matrix VBM (dot-marked region) are not plotted. Also shown are wave-function isosurface plots for the first four confined electron and hole levels. Isosurfaces are of constant value of 0.45 (green). Cross-sectional contour plots are shown on a blue-to-red (for 0.0–1.0) color scale. The crossing planes (moved from their original positions) go through the middle of the dot (shape shown in gray) and have (001) and (010) orientations.

apply the configuration-interaction (CI) method described in Ref. 40. The excitonic levels can be obtained by diagonalizing the matrix

$$\mathcal{H}_{eh,e'h'} = (E^e - E^h)\delta_{e,e'}\delta_{h,h'} - J_{eh,e'h'} + K_{eh,e'h'}, \quad (19)$$

where J and K are the Coulomb and exchange integrals:[40]

$$J_{eh,e'h'} = e^2 \sum_{\sigma_1,\sigma_2} \int\int d^3r_1 d^3r_2 \times \frac{\psi^*_{h'}(\vec{r}_1,\sigma_1)\psi^*_e(\vec{r}_2,\sigma_2)\psi_h(\vec{r}_1,\sigma_1)\psi_{e'}(\vec{r}_2,\sigma_2)}{\bar{\epsilon}(\vec{r}_1,\vec{r}_2)|\vec{r}_1 - \vec{r}_2|}, \quad (20)$$

$$K_{eh,e'h'} = e^2 \sum_{\sigma_1,\sigma_2} \int\int d^3r_1 d^3r_2 \times \frac{\psi^*_{h'}(\vec{r}_1,\sigma_1)\psi^*_e(\vec{r}_2,\sigma_2)\psi_{e'}(\vec{r}_1,\sigma_1)\psi_h(\vec{r}_2,\sigma_2)}{\bar{\epsilon}(\vec{r}_1,\vec{r}_2)|\vec{r}_1 - \vec{r}_2|}. \quad (21)$$

In the last equations, $\bar{\epsilon}(\vec{r}_1,\vec{r}_2)$ is the microscopic dielectric function and the spin degeneracy σ of the single-particle states has been explicitly taken into account.

B. Calculated electronic structure of the $In_{0.47}Ga_{0.53}As/GaAs_{0.86}P_{0.14}$ QD-IBSC

1. Confined energy levels

We show in Fig. 10 the first 20 (including spin) electron (top) and hole (bottom) dot-confined levels. On the left- and right-hand sides of Fig. 10, we show wave-function plots for the first four confined electron and hole levels. In each panel, a $|\psi_i(\vec{r})|^2$ isosurface is plotted in green, the dot shape is sketched in gray, and two contour plots are shown in a blue-to-red (0.0–1.0) scale. The first contour plot lies on the (001) plane of the supercell, passing through the base of the dot, whereas the second one is along the (010) direction and crosses the center of the dot, but is shifted from its original position for clarity. We note that, in spite of the relative small thickness of the barrier (8.4 nm at the top of the dots), the wave functions are all well localized inside the dot. As a result, no significant interdot coupling is expected to occur between the confined levels.

As can be seen in the energy-level diagram in Fig. 10, we find the typical characteristic of shallow dots[41] present also in our system: both electron and hole levels are grouped in "shells" (*s*, *p*, and *d*). Furthermore, the orbital

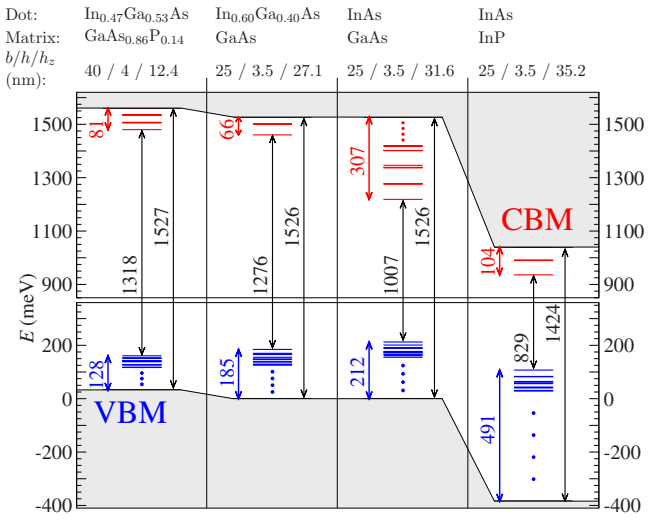

FIG. 11. (Color online) Calculated single-particle energy levels for the QD-IBSC $In_{0.47}Ga_{0.53}As/GaAs_{0.86}P_{0.14}$, compared with corresponding results obtained for other QD systems of close geometry: $In_{0.60}Ga_{0.40}As/GaAs$ (Ref. 41), InAs/GaAs (Ref. 43), and InAs/InP (Ref. 42). For each system the geometry of the dot or supercell is defined by the dot diameter b, dot height h, and vertical dot-dot separation h_z.

and Bloch character of the dot-confined states in the $In_{0.47}Ga_{0.53}As/GaAs_{0.86}P_{0.14}$ system is the same as determined in $In_{0.60}Ga_{0.40}As/GaAs$ QDs of comparable height.[41] For the former system, however, the hole states exhibit a smaller heavy hole–light hole mixing.

2. Energy separation of the IB from the band edges

We also show in Fig. 10 explicit values for the energy separations of importance for the QD-IBSC: the energy offsets of the first electron and hole dot-confined levels, $\Delta E_c = E_c - E_0^e$, and $\Delta E_v = E_0^h - E_v$, as well as the position of e_0 (the intermediate band) within the matrix band gap, corresponding to condition (iii) given in Sec. I. We see that for $In_{0.47}Ga_{0.53}As/GaAs_{0.86}P_{0.14}$ the corresponding values are $\Delta E_c = 81$ meV and $\Delta E_v = 128$ meV and the single-particle gap is $E_0^e - E_0^h = 1318$ meV. These values are very far from the ideal ones: indeed, the target for ΔE_c—which is the E_L in Fig. 1—is in the range of hundreds of meV, while $\Delta E_c/(E_0^e - E_0^h) = 0.06$ is too small as compared to the desired $E_L/(E_H + E_L)$ ratio of $\simeq 0.37$. Moreover, the h_0 offset ΔE_v is much too high as to minimize the deleterious process 4 (see Fig. 1), for which an ideal value of zero is required.

A comparison of our calculated single-particle energy levels for the QD-IBSC system $In_{0.47}Ga_{0.53}As/GaAs_{0.86}P_{0.14}$ with those of other QD systems, obtained using the same method,[41,42] is shown in Fig. 11. With respect to the $In_{0.60}Ga_{0.40}As/GaAs$ system,[41] the IB-related quantities are improved for $In_{0.47}Ga_{0.53}As/GaAs_{0.86}P_{0.14}$. Amongst the systems shown in Fig. 11, the InAs-based QDs appear to be better suited as QD-IBSC candidates. In the case of InAs/GaAs, the IB consisting of electron levels has $\Delta E_c = 307$ meV, whereas for InAs/InP the hole levels can be used to create the IB, with an offset $\Delta E_v = 491$ meV. Unfortunately, stress accumulation in both systems might prevent a successful growth of large-period samples.[17]

3. IB-related absorption spectra

We have calculated, using Eqs. (17) and (18), the absorption spectra involving the first confined electron state e_0 (S_e) within a single-particle picture. At low energies, the IB $\rightarrow$CB absorption coefficient $\sigma^{IB\rightarrow CB}(E)$ corresponds to electron intraband transitions.[44] These were thoroughly investigated in the past, owing to their importance as potential quantum dot–based infrared photodetectors.[45–47] We consider here a wider energy range than in our previous calculations using the same atomistic pseudopotential method,[44] extending far above the matrix conduction-band minimum (CBM).

Figure 12(a) shows transitions from first dot-confined level e_0 (S_e) to all other electron levels higher in energy. Our calculations were performed using a number of 300 eigenvectors of Eq. (15) for the same geometry of the system as used above. A prominent peak appears at ~ 0.03 eV, which corresponds to the dipole-allowed $e_0 \rightarrow e_{1,2}$ $(S_e \rightarrow P_e)$ transitions. This value is much smaller than ~ 0.060 eV found in InAs/GaAs and ~ 0.047 eV in $In_{0.60}Ga_{0.40}As/GaAs$.[44] Note that by comparing with the experimental results in Fig. 8(b), showing the FTIR spectra of lightly n-doped $In_{0.47}Ga_{0.53}As/GaAs_{0.86}P_{0.14}$ QDs, the predicted S_e-P_e transition lies below the low-energy cutoff. Moreover, the experimental peaks around 0.09 eV, attributed to the GaAs substrate, are indeed not found in our calculations.

Above the matrix CBM, in the energy range of 0.22–0.26 eV, a second peak, stronger than the intradot one, can be seen. This peak is nearly exclusively z polarized. An analysis of the eigenfunctions involved in the occurrence of this peak reveals that this is caused by several matrix states, strained-confined in between the dots, which are resonant with the dot. Wave-function plots of these resonant states are shown in Fig. 12(b). The presence and manifestation of such resonances in the infrared absorption is already known,[48] and they will be discussed elsewhere.[49]

Except for these strong peaks, the IB $\rightarrow$CB absorption spectrum shown in Fig. 12(a) exhibits no other strong transitions. This is a detrimental aspect in view of the IBSC functionality since condition (i) given in Sec. I requires a *strong* IB $\rightarrow$CB absorption.

We have investigated the dependence of the position of the resonant states on the vertical dot-dot separation. In doing this, the size of the QD was kept unchanged. As shown in Fig. 12(c), starting from a large dot-dot separation, a decrease in h_z results in a blueshift of the resonant peak, until it completely vanishes, at $h_z \simeq 9.0$ nm. Taking into account this h_z variation, the features shown here in the IB $\rightarrow$CB absorption might be responsible for the broad weak high-energy peaks present in Fig. 8(b).

The second process involved in the IBSC is described by the VB $\rightarrow$IB absorption coefficient $\sigma^{VB\rightarrow IB}(E)$, which has been calculated using Eq. (18), with the first confined electron state e_0 (S_e) taken now as final unoccupied state. As initial states we considered all the hole eigenfunctions starting as high as h_0 (S_h) and going well below the matrix VBM. The calculated absorption coefficient $\sigma^{VB\rightarrow IB}(E)$ for the

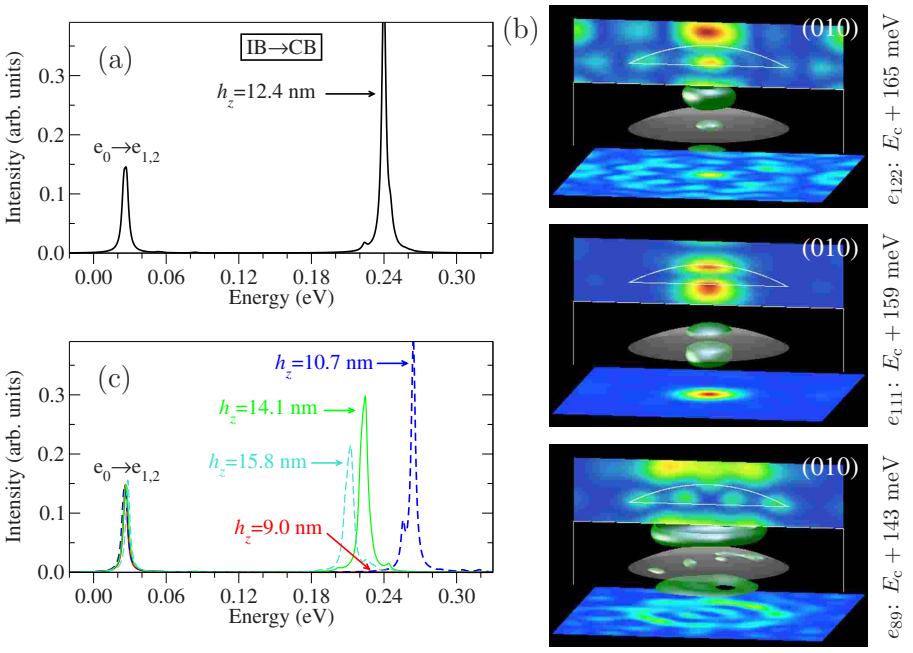

FIG. 12. (Color online) Calculated single-particle intraband absorption spectra (IB→CB) [see Eq. (17)] from the first (*S*-like) dot electron level e_0 for the QD-IBSC $In_{0.47}Ga_{0.53}As/GaAs_{0.86}P_{0.14}$. A Lorentzian with a FWHM of 2 meV was used to broaden the spectra. (a) For a dot-dot separation of h_z=12.4 nm; (b) wave-function plots of the states responsible for the peak at about 0.24 eV in panel (a). (c) Same as (a) but for different interdot separations h_z. With increasing h_z, the resonant peak moves toward lower energies, whereas for h_z=9.0 nm (red line), it completely disappears. The peak at ≃0.03 eV corresponds to the intradot $S \rightarrow P$ transition and it is not affected by variations in h_z.

benchmark QD-IBSC is shown in Fig. 13(a). We see in this spectrum three major peaks: (i) the first one, at ≃1.32 eV, corresponds to the intradot $S_h \rightarrow S_e$ transition; (ii) the second one, at ≃1.40–1.44 eV, involves dot-confined hole states located still above the matrix VBM, having the proper symmetry allowing transitions to S_e; (iii) a broad feature at ≃1.52–1.56 eV which corresponds to hole states localized in between the dots, with a shape very similar to the ones found by Mlinar *et al.*[50] for dot molecules. As can be seen from Fig. 13(b), the initial hole states involved in this (iii)-type transition are fully analogous to the dot-resonant electron states shown above.

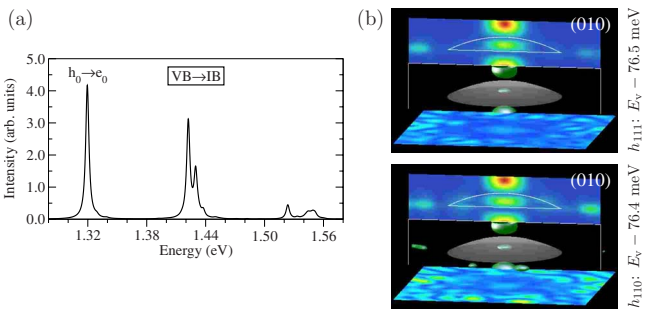

FIG. 13. (Color online) Calculated single-particle absorption spectra (VB→IB) [see Eq. (18)] for the first (*S*-like) dot electron level e_0 in the QD-IBSC system $In_{0.47}Ga_{0.53}As/GaAs_{0.86}P_{0.14}$. A Lorentzian with a FWHM of 2 meV was used to broaden the spectrum. (a) For a dot-dot separation of h_z=12.4 nm; (b) wave-function plots of the states responsible for the peak at about 1.52 eV in panel (a).

In connection with the intermediate-band concept, let us also note that the oscillator strength of the $S_h \rightarrow S_e$ transition is about 30 times larger than that of $S_e \rightarrow P_e$. A large $\sigma^{VB\rightarrow IB}(E)/\sigma^{IB\rightarrow CB}(E)$ was shown to ensure a high efficiency of the IBSC even when no photon sorting characterizes the system.[15] However, as shown above, $\sigma^{IB\rightarrow CB}(E)$ is by itself very small, such that there is practically no strong absorption overlap between the two branches IB→CB and VB→IB.

C. Calculated electronic structure of the $In_{0.47}Ga_{0.53}As/GaAs_{1-x}P_x$ QD-IBSC

Varying the P composition of the matrix will modify the strain in the system, bringing it off strain balance. While this is not a desired effect for the quality of the samples, it could be easily compensated for by a corresponding increase in the compressive strain of the dot alloy, which can be achieved by increasing its In content. On the other hand, because the benchmark QD-IBSC discussed above was found to be very far from fulfilling the IBSC criteria regarding the level offsets and the position of the IB, it would be interesting to see whether these features can be engineered toward the desired directions, the position of the IB given by condition (iii) and the reduction in ΔE_v, thus minimizing the deleterious process 4 (see Fig. 1).

1. Energy levels in $In_{0.47}Ga_{0.53}As/GaAs_{1-x}P_x$ *QD-IBSC*

Results of calculations for the $In_{0.47}Ga_{0.53}As/GaAs_{1-x}P_x$ QD system with varying P composition x are summarized in

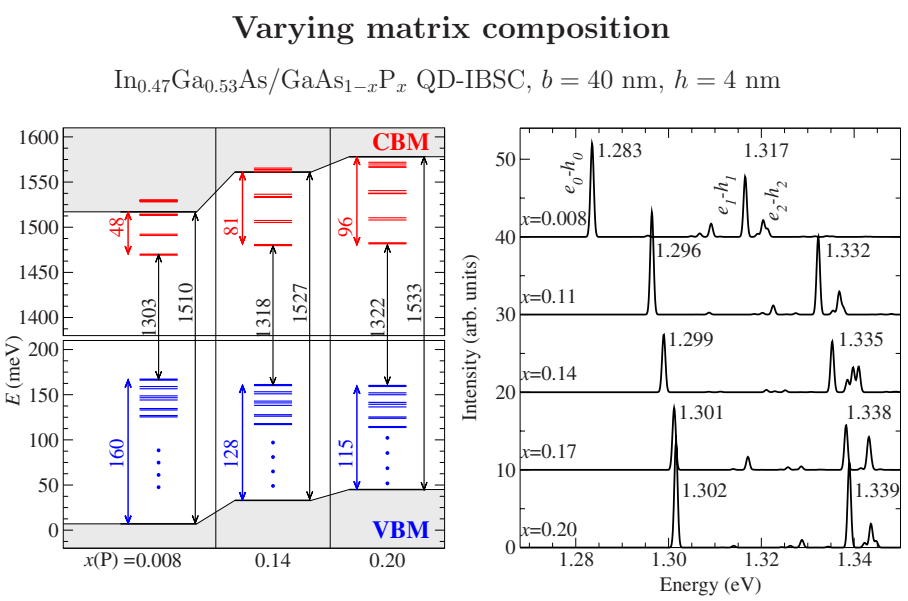

FIG. 14. (Color online) Left: Comparison of the single-particle energy levels for the QD-IBSC $In_yGa_{1-y}As/GaAs_{1-x}P_x$ with $y=0.47$ and various P contents. The energy zero corresponds to GaAs VBM. Right: Corresponding CI-calculated intradot absorption spectra.

Fig. 14. One notes that variations in P composition have only a small effect (several meV) on the *absolute* position of the dot levels (electron and holes). Because of the strong composition dependence of the matrix CBM, however, the number of confined electron levels increases with increasing x. Their offset $\Delta E_c = E_c - E_0^e$ with respect to the matrix CBM also increases with x, from 48 meV for $x=0.008$ up to 96 meV for $x=0.20$. An analogous behavior can be observed for the dot hole levels. Also in this case the absolute energetic position of the levels varies by just a few meV when x is varied, but the offset $\Delta E_v = E_0^h - E_v$ with respect to the matrix VBM decreases, mostly because of the strong variation in the latter under tensile strain. For $x=0.008$ and $x=0.20$, the corresponding values are 160 and 115 meV, respectively. Altogether, we see that increasing the P content in the matrix modifies both ΔE_c and ΔE_v in the desired directions. Nonetheless, the effect is quite small.

2. *Band edges of the* $GaAs_{1-x}P_x$ *matrix*

In order to get further insight into the ΔE_c and ΔE_v dependence on P composition, we have calculated the band edges of the $GaAs_{1-x}P_x$ matrix strained on the GaAs substrate in the following way: a supercell containing only $GaAs_{1-x}P_x$ was constructed, with its base kept fixed at the in-plane lattice constant of GaAs. The tetragonal distortion of the supercell was also fixed, at the value it had in the full system, containing the $In_{0.47}Ga_{0.53}As$ QD and WL. Using several random realizations of the $GaAs_{1-x}P_x$ alloy, the atomic positions are allowed to relax. Equation (15) is subsequently solved, providing the CBM and VBM eigenvalues.

The results of these calculations are shown in Fig. 15 [red (gray) lines]. We see that as the P content increases, the VBM rises and so does the CBM, whereas the band gap remains mostly constant.

TABLE IV. Parameters for the screened atomic pseudopotentials [in atomic units—see Eqs. (A2) and (A3)] used in this work. A plane-wave cutoff of 5 Ry was used in fitting these potentials. Also listed is the strain fitting parameter γ entering Eq. (14).

Binary:	GaAs[a] 5.6533		InAs[a] 6.0583		InP[b] 5.8687		GaP 5.4505	
Lattice constant: (Å)	Ga	As	In	As	In	P	Ga	P
a_0	432960	10.9386	644.130	26.4682	5012.05	21.9157	667.899	37.8781
a_1	1.78424	3.09050	1.51263	3.03129	1.85558	2.92152	2.53678	2.73210
a_2	18880.6	1.10396	15.2009	1.24642	88.8570	1.21902	35.9091	1.33813
a_3	0.20810	0.23304	0.35374	0.42129	0.74194	0.35537	0.22279	0.39957
a_{SO}	0.0460	0.0976	0.4800	0.0976	0.0480	0.0140	0.0137	0.0088
γ	2.56392	0.00000	2.18215	0.00000	0.48000	0.01404	1.06625	0.00876

[a]Reference 38.
[b]Reference 42.

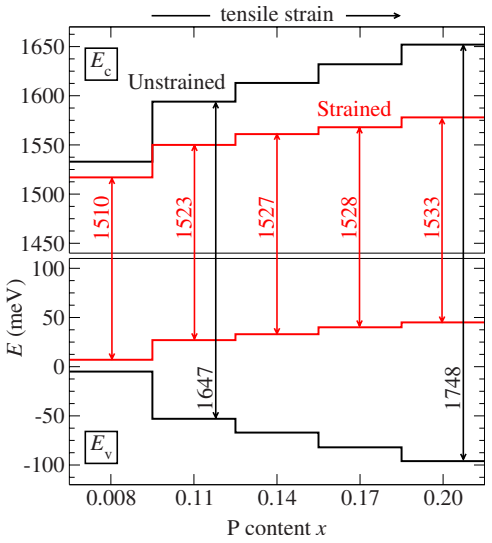

FIG. 15. (Color online) Strained [red (gray)] and unstrained (black) band edges E_v and E_c for the $GaAs_{1-x}P_x$ matrix. The former were obtained by solving Eq. (15) for a system with the interlayer spacing and strain borrowed from the VFF-relaxed supercell of the matrix+WL+dot system epitaxially grown on GaAs(001) substrate. Energy zero corresponds to GaAs VBM.

It is important to mention that this trend includes two effects: (i) the change in VBM and CBM of $GaAs_{1-x}P_x$ with x in the absence of strain (black lines in Fig. 15) and (ii) the combined chemical and strain effect [red (gray) line]. The chemical effect alone moves E_v down and E_c up as x increases.

Comparing the strained and unstrained band edges in Fig. 15, the effect of the strain is quite pronounced: the strained CBM (VBM) is systematically lower (higher) in energy than its corresponding unstrained value. For the VBM, we even see a change in slope with increasing x as a consequence of the elastic deformation potentials. As a result, the band gap of $GaAs_{0.86}P_{0.14}$ increases slightly, from 1510 meV for $x=0.008$ to 1533 meV for $x=0.2$, much less than it would be expected from pure chemical offsets only.

3. Intradot absorption spectra

By means of the CI approach described in Ref. 40, we have calculated the intradot absorption spectra for the $In_{0.47}Ga_{0.53}As/GaAs_{1-x}P_x$ system. A number of 12 electron and hole states (including spin degeneracy) have been considered, corresponding to S-S and P-P transitions. The results of the calculations, averaged over the light polarization, are shown in Fig. 14(b). As suggested already by the single-particle results, the exciton peaks (dominant S_e-S_h and P_e-P_h) show a monotonic, nonlinear dependence on x(P). The Coulomb integrals deduced from the CI calculations are about 20 meV for the S levels, and 16 meV for the P levels, nearly independent of x(P) and the alloy fluctuations.

D. Calculated electronic structure of the $In_yGa_{1-y}As/GaAs_{0.86}P_{0.14}$ QD-IBSC

In varying the P composition of the matrix, our main interest was to see whether the intermediate-band-related characteristics of the system (energy offsets and differences) can be improved. A similar purpose is followed in this section but this time by modifying the In content y(In) of the dot material $In_yGa_{1-y}As$ while simultaneously keeping the matrix composition constant as $GaAs_{0.86}P_{0.14}$.

The results of the calculations are shown in Fig. 16(a) for the single-particle levels and Fig. 16(b) for the CI-calculated intradot absorption spectra. Since in the bulk $In_yGa_{1-y}As$ alloy the band gap decreases with increasing In composition, the increased confinement observed in Fig. 16(a) for the QD system when moving from y(In)=0.44 to y(In)=0.50 was to be expected. We see, however, that the dependence of the energy differences on y(In) is almost linear, in this composition range, unlike the nonlinear dependence on x(P) observed above. A similar behavior is seen also in the exciton peak positions [Fig. 16(b)].

In connection with the IBSC criteria, we note that the electron levels' offset ΔE_c, although increasing with y(In), is still too small. Even worse, the hole levels' offset ΔE_v, which should be minimized, also increases with y(In).

V. COMPARISON WITH EXPERIMENT AND DISCUSSION

When comparing the theoretical results with the experimental data, we need to bear in mind that, while the calculations were performed using low-temperature-fitted pseudo-

TABLE V. Fitted bulk electronic properties for GaP using the screened atomic pseudopotentials (PPs) of this work. All energies are given relative to the unstrained $E_{\Gamma_{15v}}$. m_e^*, m_{hh}^*, and m_{lh}^* are the effective masses for the electron, the heavy hole, and the light hole; $a_{\Gamma_{1c}}$ and $a_{\Gamma_{15v}}$ are the hydrostatic deformation potentials at the Γ_{1c} and Γ_{15v} levels; b is the biaxial deformation potential; and Δ_0 is the spin-orbit splitting at Γ_{15v}.

Property	PP	Target
$E_{\Gamma_{15v}}$ (eV)	−6.101	−6.099[a]
$E_{\Gamma_{1c}}$ (eV)	2.743	2.895[b]
$E_{X_{1c}}$ (eV)	2.342	2.350[b]
$E_{X_{3c}}$ (eV)	2.936	2.705[b]
$E_{X_{5v}}$ (eV)	−3.097	−2.700[b]
$E_{L_{1c}}$ (eV)	2.732	2.637[b]
$E_{L_{3v}}$ (eV)	−1.329	−1.200[b]
m_e^*	0.091	0.093[c]
$m_{hh}^*[100]$	0.316	0.326[c]
$m_{hh}^*[111]$	1.653	0.645[c]
$m_{lh}^*[100]$	0.153	0.199[c]
$m_{lh}^*[111]$	0.110	0.153[c]
$a_{\Gamma_{1c}}$	−7.603	−8.83[d]
$a_{\Gamma_{15v}}$	−0.609	−0.58[d]
b	−3.206	−1.60[c]
Δ_0 (eV)	0.081	0.08[b,c]

[a]Reference 54.
[b]References 26 and 27.
[c]Reference 51.
[d]Reference 55.

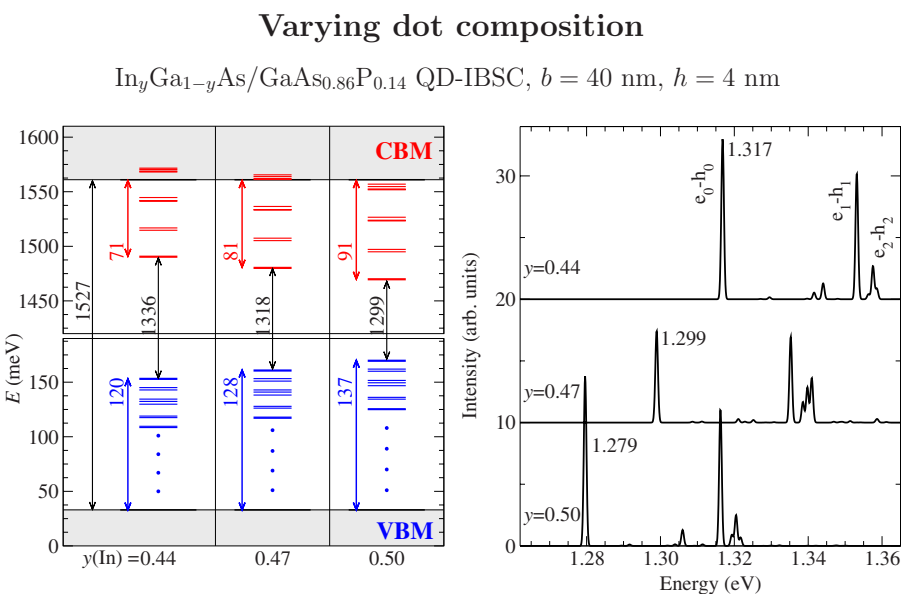

FIG. 16. (Color online) Left: Comparison of the single-particle energy levels for the QD-IBSC $In_yGa_{1-y}As/GaAs_{1-x}P_x$ with $x=0.14$ and various In concentrations in the dot. The energy zero corresponds to GaAs VBM. Right: Corresponding CI-calculated intradot absorption spectra.

potentials, the experiments were carried out at room temperature. Thus, a direct comparison is possible only after applying a temperature correction of $\simeq 70-100$ meV for the optical gap.[33,51]

The current-voltage measurements presented in Fig. 5 (see Sec. III) show an increase in the open-circuit voltage V_{oc} when the P composition has been varied from $x=0.008$ to $x=0.14$. The maximum V_{oc} increase expected from increasing the average band gap of the absorbing region is 0.17 eV, which corresponds to the difference in band gap expected between unstrained $GaAs_{0.83}P_{0.17}$, 1.71 eV, and $GaAs_{0.992}P_{0.008}$, 1.54 eV. However, in our strain-balanced QD cells, the $GaAs_{1-x}P_x$ barrier layers are under tensile strain and this lowers the band gap with respect to the unstrained alloy, as could be seen above (Fig. 15). Therefore, a reduced V_{oc} increase should be expected from the increased level of P composition in the tensile-strained barrier layers.

If a large VB offset is present, it leads to the introduction of a high number of closely spaced hole levels into the QD, with a separation smaller than k_BT that can overlap with the barrier layer VB continuum. This can enable easy, rapid relaxation of holes, through phonon interaction, from the VB continuum to the hole levels in the QDs. This will result in a reduction in the V_{oc} of the cell of close to the value of the VB offset. The theoretical results for the VB offsets have shown that as the P concentration in the barrier layers is increased, the VB offset is reduced. This effect could also contribute to the higher V_{oc} observed in the close to strain-balanced $In_{0.47}Ga_{0.53}As/GaAs_{1-x}P_x$ QD cells with $x=0.14$ and $x=0.18$.

The experimental results for PL (Fig. 6) and PC (Fig. 7) discussed in Sec. III are summarized in Table III. From these data, we see that the first peak in PC moves from 1.16 eV for $x(P)=0.008$ to 1.23 eV for $x(P)=0.14$, i.e., a redshift of $\simeq 70$ meV. A further increase in P composition, to $x(P)=0.18$, no longer changes the transition energies. The PL measurements, which give systematically lower (about 30–50 meV) values of the ground exciton, show a similar nonlinear dependence on $x(P)$ of the interband transition energies. This behavior is correctly reproduced by our calculations (see Fig. 14), although the theoretical results predict a smaller shift, $\simeq 16$ meV, upon changing the P composition from 0.008 to 0.14.

A second peak appears in the $x=0.008$ PC data (not resolved by PL), attributed to the P_e-P_h exciton. Relative to the ground exciton S_e-S_h, it is 0.06 eV higher in energy. Using the main excitonic contribution to each peak [Eq. (19), results shown in Fig. 14(b)], we see that the theoretically predicted splitting is 0.036 eV. Based on these comparisons, we conclude that our calculations describe reasonably well the main trends observed in the QD-IBSC with varying matrix composition.

Photocurrent measurements have also shown that at temperatures greater than $\simeq 200$ K, most of the carriers created by interband absorption are expected to escape from the QDs and, consequently, the PC spectra should give a good representation of the absorption spectra of the QD samples. This means that our devices are not working as true intermediate-band solar cells because carrier escape from the QDs is mainly by thermal excitation and not optical excitation at room temperature. Our calculations of the intraband absorption (Fig. 12), giving reasonably good agreement with the FTIR measurements [Fig. 8(b)], suggest that this is due to the small energy offset of the dot-confined electron levels, thus being far from condition (iii) of the IBSC and favoring, instead of diminishing, the deleterious process 1′ [see Fig. 1(c)].

Our theoretical investigations have shown that an increased P composition of the matrix, causing an increase in the tensile stress, modifies both the electron *and* hole energy offsets, ΔE_c and ΔE_v, in a way favorable for the IBSC. An increased In composition of the dot, implying a larger com-

pressive strain, acts beneficial only to the electron levels, increasing their energy offset ΔE_c while simultaneously increasing ΔE_v. The rate of ΔE_v increase with y(In) is smaller than its decrease due to a larger x(P). We suggest that, while the present $In_yGa_{1-y}As/GaAs_{1-x}P_x$ system does not seem to be appropriate for IBSC, further engineering might bring it closer to the ideal energy offsets required by intermediate-band efficiency predictions.

VI. CONCLUSIONS

We have experimentally demonstrated that strain balance can be a highly effective way to obtain multilayer QD structures with good size uniformity, high optical quality, and low dislocation density. Both continuum-elasticity and atomic-elasticity calculations have been applied to determine the strain-balance condition for $In_{0.47}Ga_{0.53}As/GaAs_{1-x}P_x$ strained-layer superlattices grown on (001) GaAs substrates, for an $In_{0.47}Ga_{0.53}As$ layer thickness of 6 ML, just above the critical thickness for Stranski-Krastanov growth on GaAs. The results of the two different calculation procedures are very close between $x=0.12$ and $x=0.18$ but diverge by 10% or more outside of this narrow composition range. We successfully obtained high-quality strain-balanced $In_{0.47}Ga_{0.53}As/GaAs_{1-x}P_x$ QD superlattices grown on (113)B GaAs substrates. Disappointingly, the performance of *pin* solar cells incorporating such QD superlattices in the intrinsic region was worse than a GaAs *pin* control cell with the identical device structure without any QDs. Modeling of the optical and electronic properties of $In_yGa_{1-y}As/GaAs_{1-x}P_x$ QD structures, using an atomistic pseudopotential method, gave close agreement with the experimentally determined properties of the QD structures. The calculations and experiments revealed that the electronic structure and absorption properties of the studied system are, unfortunately, far from fulfilling the conditions for an efficient QD-IBSC. To conclude, alternative QD/barrier material combinations are required that have an electronic structure and absorption properties more suitable for a QD-IBSC systems.

ACKNOWLEDGMENTS

The work of V.P., M.C.H., and A.G.N. was funded by the U.S. Department of Energy through NREL's Laboratory Directed Research and Development program. The collaboration with A.Z. and G.B. was funded by the U.S. Department of Energy Office of Science, Basic Energy Science, under Contract No. DE-AC36-99GO10337 to NREL. The authors gratefully acknowledge P. Dippo for the room-temperature PL measurements, L. M. Gedvilas for the FTIR measurements, and J. S. Ward for device processing.

APPENDIX: PSEUDOPOTENTIALS

We used for the screened, unstrained pseudopotentials entering Eq. (14) the expression proposed by Williamson *et al.*:[38]

$$v_\alpha(\vec{r},0) = \frac{1}{\Omega}\sum_{\vec{q}} e^{i\vec{q}\cdot\vec{r}} v_\alpha(q), \tag{A1}$$

with

$$v_\alpha(q) = a_{0,\alpha}\frac{q^2 - a_{1,\alpha}}{a_{2,\alpha}e^{a_{3,\alpha}q^2} - 1}. \tag{A2}$$

The nonlocal spin-orbit coupling potential term in Eq. (15) has been calculated using the formula[52]

$$\hat{V}_{\mathrm{NL}} = a_{\mathrm{SO}}\sum_{i,j} |i\rangle B(i,j)\langle j|, \tag{A3}$$

where $|i\rangle$ and $|j\rangle$ are reference functions and $B(i,j)$ is a matrix representation of the spin-orbit interaction, $B(i,j) = \langle i|\vec{L}\vec{S}|j\rangle$, with $\vec{L}$ and $\vec{S}$ as the spatial angular momentum operator and spin operator, respectively.

The local pseudopotentials $v_\alpha(\vec{r},0)$ are determined by requiring that the bulk GaAs, InAs, GaP, and InP described by $v_\alpha(\vec{r},0)$ fit experimental and LDA data including band energies at high-symmetry points, effective masses, and hydrostatic and biaxial deformation potentials as well as the unstrained valence-band offsets between the various binary compounds. For InAs/GaAs (Ref. 38) and InAs/InP,[42] fitted pseudopotentials were already available in the literature; for GaAs/GaP, in turn, a set of data is proposed here.[53] We give in Table IV the parameters for all the empirical pseudopotentials used in this work.

We also list, in Table V, the target values used to fit the pseudopotentials and the corresponding fitted values for the GaP binary. Consistency with previously determined pseudopotentials[38,42] was ensured by taking the same kinetic-energy scaling factor $\beta=1.23$ [see Eq. (15)].

*Present address: Max-Planck-Institut für Festkörperforschung, Heisenbergstraße 3, D-70569 Stuttgart, Germany.

[1] *Next Generation Photovoltaics: High Efficiency through Full Spectrum Utilization*, Series in Optics and Optoelectronics, edited by A. Martí and A. Luque (Institute of Physics, Bristol, 2004).
[2] M. A. Green, *Third Generation Photovoltaics: Advanced Solar Energy Conversion* (Springer-Verlag, Heidelberg, 2003).
[3] A. Luque and A. Martí, Phys. Rev. Lett. **78**, 5014 (1997).
[4] P. Palacios, J. J. Fernández, K. Sánchez, J. C. Conesa, and P. Wahnón, Phys. Rev. B **73**, 085206 (2006).
[5] C. Tablero, Phys. Rev. B **74**, 195203 (2006).
[6] P. Palacios, K. Sánchez, J. C. Conesa, J. J. Fernández, and P. Wahnón, Thin Solid Films **515**, 6280 (2007).
[7] P. Palacios, I. Aguilera, K. Sánchez, J. C. Conesa, and P. Wahnón, Phys. Rev. Lett. **101**, 046403 (2008).
[8] K. M. Yu, W. Walukiewicz, J. Wu, W. Shan, J. W. Beeman, M. A. Scarpulla, O. D. Dubon, and P. Becla, Phys. Rev. Lett. **91**, 246403 (2003).
[9] K. M. Yu, W. Walukiewicz, J. W. Ager III, D. Bour, R. Farshchi,

O. D. Dubon, S. X. Li, I. D. Sharp, and E. E. Haller, Appl. Phys. Lett. **88**, 092110 (2006).
[10] A. Luque, A. Martí, C. Stanley, N. López, L. Cuadra, D. Zhou, J. L. Pearson, and A. McKee, J. Appl. Phys. **96**, 903 (2004).
[11] S. Suraprapapich, S. Thainoi, S. Kanjanachuchai, and S. Panyakeow, Sol. Energy Mater. Sol. Cells **90**, 2968 (2006).
[12] R. B. Laghumavarapu, A. Moscho, A. Khoshakhlagh, M. El-Emawy, L. F. Lester, and D. L. Huffaker, Appl. Phys. Lett. **90**, 173125 (2007).
[13] R. B. Laghumavarapu, M. El-Emawy, N. Nuntawong, A. Moscho, L. F. Lester, and D. L. Huffaker, Appl. Phys. Lett. **91**, 243115 (2007).
[14] S. M. Hubbard, C. D. Cress, C. G. Bailey, R. P. Raffaelle, S. G. Bailey, and D. M. Wilt, Appl. Phys. Lett. **92**, 123512 (2008).
[15] L. Cuadra, A. Martí, and A. Luque, IEEE Trans. Electron Devices **51**, 1002 (2004).
[16] V. A. Shchukin, N. N. Ledentsov, and D. Bimberg, *Epitaxy of Nanostructures* (Springer, New York, 2004).
[17] A. Martí, N. López, E. Antolín, E. Cánovas, A. Luque, C. R. Stanley, C. D. Farmer, and P. Díaz, Appl. Phys. Lett. **90**, 233510 (2007).
[18] A. Luque, A. Martí, N. López, E. Antolín, E. Cánovas, C. Stanley, C. Farmer, L. J. Caballero, L. Cuadra, and J. L. Balenzategui, Appl. Phys. Lett. **87**, 083505 (2005).
[19] N. J. Ekins-Daukes, K. Kawaguchi, and J. Zhang, Cryst. Growth Des. **2**, 287 (2002).
[20] L. Bhusal and A. Freundlich, Phys. Rev. B **75**, 075321 (2007).
[21] J. W. Matthews and A. E. Blakeslee, J. Cryst. Growth **32**, 265 (1976).
[22] J. Tatebayashi, N. Nuntawong, Y. C. Xin, P. S. Wong, S. H. Huang, C. P. Hains, L. F. Lester, and D. L. Huffaker, Appl. Phys. Lett. **88**, 221107 (2006).
[23] P. N. Keating, Phys. Rev. **145**, 637 (1966).
[24] R. M. Martin, Phys. Rev. B **1**, 4005 (1970).
[25] K. Kim, P. R. C. Kent, A. Zunger, and C. B. Geller, Phys. Rev. B **66**, 045208 (2002).
[26] *Semiconductors: Group IV and III-V Compounds*, Landolt-Börnstein, New Series, Group III Vol. 17, edited by O. Madelung (Springer, Berlin, 1982).
[27] *Semiconductors: Intrinsic Properties of Group IV Elements and III-V, II-VI and I-VII Compounds*, Landolt-Börnstein, New Series, Group III Vol. 22, edited by O. Madelung (Springer, Berlin, 1987).
[28] D. Sander, Rep. Prog. Phys. **62**, 809 (1999).
[29] L. De Caro and L. Tapfer, Phys. Rev. B **51**, 4374 (1995).
[30] L. De Caro and L. Tapfer, Phys. Rev. B **51**, 4381 (1995).
[31] A. G. Norman, M. C. Hanna, P. Dippo, D. H. Levi, R. C. Reedy, J. S. Ward, and M. M. Al-Jassim, Proceedings of 31st IEEE Photovoltaic Specialists Conference, Lake Buena Vista, Florida (IEEE, New York, 2005), pp. 43–48.
[32] Y. C. Zhang, A. Pancholi, V. G. Stoleru, M. C. Hanna, and A. G. Norman, Appl. Phys. Lett. **91**, 223109 (2007).
[33] W.-H. Chang, T. M. Hsu, C. C. Huang, S. L. Hsu, C. Y. Lai, N. T. Yeh, T. E. Nee, and J.-I. Chyi, Phys. Rev. B **62**, 6959 (2000).
[34] P. W. Fry *et al.*, Phys. Rev. B **62**, 16784 (2000).
[35] A. Patanè, A. Levin, A. Polimeni, L. Eaves, P. C. Main, M. Henini, and G. Hill, Phys. Status Solidi B **224**, 41 (2001).
[36] J. Phillips, K. Kamath, X. Zhou, N. Chervala, and P. Bhattacharya, Appl. Phys. Lett. **71**, 2079 (1997).
[37] J. Phillips, P. Bhattacharya, S. W. Kennerly, D. W. Beekman, and M. Dutta, IEEE J. Quantum Electron. **35**, 936 (1999).
[38] A. J. Williamson, L. W. Wang, and A. Zunger, Phys. Rev. B **62**, 12963 (2000).
[39] L.-W. Wang and A. Zunger, Phys. Rev. B **59**, 15806 (1999).
[40] A. Franceschetti, H. Fu, L. W. Wang, and A. Zunger, Phys. Rev. B **60**, 1819 (1999).
[41] G. A. Narvaez, G. Bester, and A. Zunger, J. Appl. Phys. **98**, 043708 (2005).
[42] M. Gong, K. Duan, C.-F. Li, R. Magri, G. A. Narvaez, and L. He, Phys. Rev. B **77**, 045326 (2008).
[43] L. He and A. Zunger, Phys. Rev. B **73**, 115324 (2006).
[44] G. A. Narvaez and A. Zunger, Phys. Rev. B **75**, 085306 (2007).
[45] J. Phillips, K. Kamath, and P. Bhattacharya, Appl. Phys. Lett. **72**, 2020 (1998).
[46] S. Maimon, E. Finkman, G. Bahir, S. E. Schacham, J. M. Garcia, and P. M. Petroff, Appl. Phys. Lett. **73**, 2003 (1998).
[47] D. Pan, E. Towe, and S. Kennerly, Appl. Phys. Lett. **73**, 1937 (1998).
[48] P. Lelong, S. W. Lee, K. Hirakawa, and H. Sakaki, Physica E (Amsterdam) **7**, 174 (2000).
[49] V. Popescu, G. Bester, and A. Zunger (unpublished).
[50] V. Mlinar, M. Tadić, and F. M. Peeters, Phys. Rev. B **73**, 235336 (2006).
[51] I. Vurgaftman, J. R. Meyer, and L. R. Ram-Mohan, J. Appl. Phys. **89**, 5815 (2001).
[52] L.-W. Wang, J. Kim, and A. Zunger, Phys. Rev. B **59**, 5678 (1999).
[53] J. W. Luo (unpublished).
[54] S.-H. Wei and A. Zunger, Appl. Phys. Lett. **72**, 2011 (1998).
[55] S.-H. Wei and A. Zunger, Phys. Rev. B **60**, 5404 (1999).